Development of Sinter-Resistant Core-Shell LaMnxFe1-xO3@mSiO(2) Oxygen Carriers for Chemical Looping Combustion

4 AUTHORS:

Zahra Sarshar
Polytechnique Montréal
7 PUBLICATIONS **63** CITATIONS

SEE PROFILE

Zhenkun Sun
Natural Resources Canada
38 PUBLICATIONS **1,866** CITATIONS

SEE PROFILE

Dongyuan Zhao
Monash University (Australia)
526 PUBLICATIONS **27,611** CITATIONS

SEE PROFILE

Serge Kaliaguine
Laval University
498 PUBLICATIONS **12,747** CITATIONS

SEE PROFILE

Development of Sinter-Resistant Core−Shell LaMn$_x$Fe$_{1−x}$O$_3$@mSiO$_2$ Oxygen Carriers for Chemical Looping Combustion

Zahra Sarshar,[†] Zhenkun Sun,[‡] Dongyuan Zhao,[‡] and Serge Kaliaguine*[,†]

[†]Department of Chemical Engineering, Laval University, Québec City, Québec G1V 0A6, Canada
[‡]Department of Chemistry, Advanced Materials Laboratory, Fudan University, Shanghai 200433, People's Republic of China

S Supporting Information

ABSTRACT: This work investigates the possibility of using LaMn$_{0.7}$Fe$_{0.3}$O$_{3.15}$@mSiO$_2$ as oxygen carriers for chemical looping combustion (CLC). CLC is a new combustion technique with inherent separation of CO$_2$ from atmospheric N$_2$. LaMn$_{0.7}$Fe$_{0.3}$O$_{3.15}$@mSiO$_2$ core−shell materials were prepared by coating a layer of mesostructured silica around the agglomerated perovskite particles. The oxygen carriers were characterized using different methods, such as X-ray diffraction (XRD), scanning electron microscopy (SEM), transmission electron microscopy (TEM), N$_2$ sorption, hydrogen temperature-programmed reduction (H$_2$-TPR), and temperature-programmed desorption of oxygen (TPD-O$_2$). The reactivity and stability of the carrier materials were tested in a special reactor, allowing for short contact time between the fluidized carrier and the reactive gas [Chemical Reactor Engineering Centre (CREC) fluidized riser simulator]. Multiple reduction−oxidation cycles were performed. TEM images of the carriers showed that a perfect mesoporous silica layer was formed around samples with 4, 32, and 55 nm in thickness. The oxygen carriers having a core−shell structure showed higher reactivity and stability during 10 repeated redox cycles compared to the LaMn$_{0.7}$Fe$_{0.3}$O$_{3.15}$ core. This could be due to a protective role of the silica shell against sintering of the particles during repeated cycles under CLC conditions. The agglomeration of the particles, which occurred at high temperatures during CLC cycles, is more controllable in the core−shell-structured carriers, as confirmed by SEM images. XRD patterns confirmed that the crystal structure of all perovskites remained unchanged after multiple redox cycles. Methane conversion and partial conversion to CO$_2$ were observed to increase with the contact time between methane and the carrier. Indeed, more oxygen from the carrier surface, grain boundaries, and even from the bulk lattice was released to react with methane. Upon rising the contact time, less CO was formed, which is desirable for CLC application. Increasing the reaction temperature and methane partial pressure lead to enhanced conversions of CH$_4$ under CLC conditions.

1. INTRODUCTION

The threat of global warming has made it urgent to develop the technologies for producing power without the release of greenhouse gases, such as CO$_2$. Fossil-fuel-combustion-based power plants are responsible for roughly 40% of the global CO$_2$ emission.[1] Because of high cost of alternative energy sources, the use of fossil fuels is still essential. Therefore, cost-effective CO$_2$ capture from fossil fuel uses and subsequent sequestration technologies need to be developed. Current CO$_2$ separation technologies, such as post-combustion, oxy-fuel combustion, and pre-combustion, used in industry lead to significant increases in the cost of electricity. A large portion of the energy that these technologies generate is consumed to separate gases, and as a result, the overall efficiency of a power plant is reduced.[2] Chemical looping combustion (CLC) is a rather new combustion technology that has recently gained increased attention. This efficient technology was initially proposed to increase the thermal efficiency of power plants.[3,4] It was then found as having inherent advantages for CO$_2$ separation compared to the conventional technologies, where the CO$_2$ produced is diluted with atmospheric nitrogen. The CLC system consists of two fluidized-bed reactors: an air reactor (AR) and a fuel reactor (FR) (see Figure 1). The fuel is oxidized in the FR using metal oxides as the oxygen carrier. The reduced metal oxides are returned to the AR, where they are reoxidized by air. At the exit of the AR, the oxidized carrier is
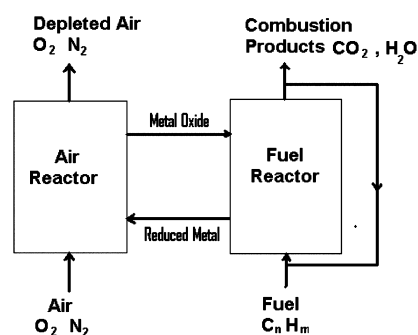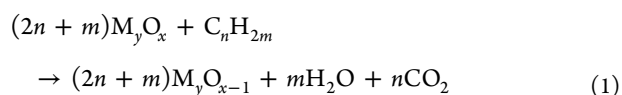

Figure 1. Principle of CLC.

separated by a cyclone and returned to the FR for the next cycle. The net chemical reaction and energy release is identical to that of the conventional combustion of the fuel.[5] In the fuel reactor, the fuel is oxidized according to reaction 1.
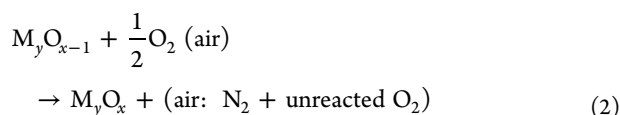
$$(2n + m)M_yO_x + C_nH_{2m}$$
$$\rightarrow (2n + m)M_yO_{x−1} + mH_2O + nCO_2 \qquad (1)$$

In the air reactor, the oxygen carrier is reoxidized in air according to reaction 2.

$$M_yO_{x-1} + \frac{1}{2}O_2 \text{ (air)}$$

$$\rightarrow M_yO_x + (\text{air: } N_2 + \text{unreacted } O_2) \qquad (2)$$

The exhaust stream of the FR consists mainly of CO_2 and H_2O. The H_2O can be easily condensed, resulting in a pure CO_2 gas, which can then be pressurized and sequestered, while the outlet gas stream of the air reactor contains nitrogen and unreacted oxygen.

CLC has great potential as a next-generation combustion technology because it has the inherent advantage to produce near-zero CO_2 emissions with a minor effect on the overall efficiency of power plants. Indeed, this process efficiency will be strongly dependent upon the performance and stability of the oxygen carrier. CLC also minimizes NO_x formation because the fuel burns in the fuel reactor in an air-free environment and the reduced oxygen carrier is reoxidized in the air reactor in the absence of a fuel, at comparatively lower temperatures.[6]

Several designs have been tested concerning the CLC reactor design, such as an alternating fixed-bed reactor, two interconnected fluidized-bed reactors, or a rotating-bed reactor.[7,8] The application of CLC at large scale highly depends upon the availability of a suitable oxygen carrier material. Important criteria for oxygen carriers are high reactivity in both reduction by fuel gas and oxidation by oxygen in the air, high stability under repeated reduction−oxidation cycles at high temperatures, and high resistance to attrition, fragmentation, and agglomeration. Additionally, it is also required that the metal oxide be cheap and environmentally friendly.[9−11] Several supported transition-metal oxides have been investigated as oxygen carrier materials in the literature, such as NiO,[12−14] CuO,[15−18] Fe_2O_3,[11,19,20] and Mn_3O_4.[7,21] These oxygen carriers have shown different advantages and disadvantages for CLC applications; however, they all suffer from chemical and/or thermal stresses placed on these materials during repeated reduction−oxidation cycles. The mentioned metal oxides have shown some problematic issues during repeated redox cycles, including a low oxygen ratio, mass fraction of oxygen in a carrier (e.g., in the case of Mn_3O_4), loss of stability as a result of appearing as a non-reducible species because of the interaction between metal oxides and supports (e.g., in the case of NiO), or agglomeration of particles and coke formation (e.g., in the case of Fe_2O_3 and CuO). These limit the carrier efficiency during CLC cycles and yield thermodynamic limitations of metal oxides, which lead to incomplete combustion products, such as CO (e.g., in the case of NiO).[5,7,12,13,16] Recently, Gayán et al.[17] have studied the use of Cu-based oxygen carriers prepared by impregnation on different supports for CLC and found that CuO supported on γAl_2O_3 modified with NiO exhibited good properties, such as high reactivity together with high mechanical durability and absence of agglomeration.

In our previous work,[22] we have studied the feasibility of using perovskite mixed oxides as oxygen carrier materials. The wrong perception that perovskites are too expensive for CLC application was dealt with in this previous contribution.[22] Indeed, there are a few studies using perovskites as oxygen carriers for CLC.[23−25] Bakken et al.[26] have found that perovskite-based phases in the Ca−Mn−O system are able to tolerate a large degree of oxygen non-stoichiometry without decomposing. Oxygen release and uptake in these mixed

valency materials occur by oxygen diffusion rather than cation diffusion (e.g., in the case of Mn_3O_4 and Fe_2O_3 oxides), thus potentially allowing for lowered CLC process temperatures, although a higher temperature is preferable to increase the turbine efficiency for power generation.[27] Two types of perovskites, $LaCoO_3$ and $LaMnO_3$, prepared by reactive grinding and nanocasting methods were investigated as oxygen carriers for CLC application in our previous study.[22] Both perovskites, particularly $LaMnO_3$, demonstrated high reactivity and stability of CH_4 combustion under CLC conditions. The coke formation was negligibly small, but some agglomeration of particles was observed after repeated redox cycles. In this study, the system of perovskite@SiO_2 core−shell nanoparticles (CSNs) was selected to be prepared, characterized, and tested as oxygen carrier materials for CLC. One of the emerging classes of nanostructured materials is core−shell nanoparticles, which attracted broad interest in recent years in optical, electronic, magnetic, catalytic, and medical applications.[28,29] The core−shell nanomaterial is broadly defined as a core and shell of different matters in close interaction, including inorganic/organic, inorganic/inorganic, organic/organic, or inorganic/biological combinations.[28−30] CSNs provide this opportunity to control the size of nanoparticles in both core and shell areas. Furthermore, they are found to be efficient materials to control and prevent the sintering and aggregation of nanoparticles in catalytic applications; for instance, one strategy is to encapsulate the active nanoparticle catalysts within porous silica shells.[31,32] Park et al.[31] prepared Pd@SiO_2 core@shell nanoparticles with Pd cores in uniform shape and monodisperse of about 4.2 nm and silica shell with 10 nm in thickness. They have studied this carbon nanoparticle (CNP) for CO oxidation and acetylene hydrogenation and found improved activity and minimal sintering (up to 700 °C) compared to traditional silica-supported Pd. Joo et al.[33] demonstrated that Pt@SiO_2 core@shell nanoparticles maintained their core−shell configurations up to 750 °C and exhibited high catalytic activity for ethylene hydrogenation and CO oxidation. They found that the mesoporous silica shells isolate the catalytically active Pt cores and prevent the possibility of sintering of core particles during catalytic reactions at high temperatures. Recently, Epherre et al.[34] have uniformly coated $La_{0.82}Sr_{0.18}MnO_{3+\delta}$ perovskite nanoparticles with a mean crystallite size of 22 nm with a 5 nm thick silica shell, employing a procedure derived from Stöber's method. They have applied this core−shell material in magnetic fluid hyperthermia (MFH), which is a complementary route to chemotherapy and radiotherapy of tumor cells. They have found that no aggregate was detected, and nanoparticles obtained a size and heating behavior in agreement with MFH requirements. Park et al.[35] have recently investigated the use of Fe_3O_4@SiO_2 core−shell nanoparticles as a catalyst for CO oxidation as well as oxygen carriers for CLC. They have prepared this silica-encapsulated iron oxide via a reverse micelle microemulsion and obtained core−shell nanoparticles with a shell size of about 4.5 nm in thickness. They have shown that the Fe_3O_4@SiO_2 nanoparticles retained their physical, chemical, and magnetic properties following thermal treatment up to 700 °C in air. Furthermore, the core magnetite within the silica shell is resistant to sintering and a bulk phase transition at temperatures as high as 700 °C.

There may be concern with regard to the cost of preparing core−shell materials, especially when the targeted application is conversion of fossil fuels. Because such materials have not yet
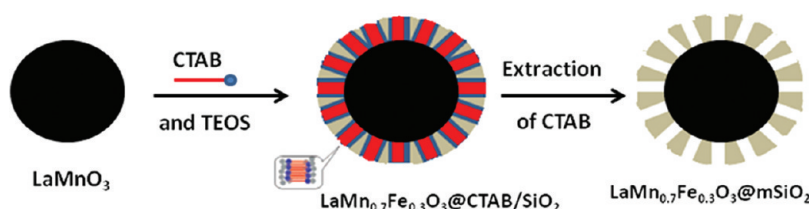
Figure 2. Formation of $LaMn_{0.7}Fe_{0.3}O_{3.15}@mSiO_2$ core@shell nanoparticles.

been synthesized at industrial scale, the cost of coating core particles is not yet established. Some technology of liquid fluidized-bed coating is currently under study in our laboratory. The preparation of thin-coated particles may end up to be commercially attractive.

In this paper, we report the synthesis of $LaMn_{0.7}Fe_{0.3}O_{3.15}@mSiO_2$ core−shell nanocomposites via a surfactant-templating process, in which $LaMn_{0.7}Fe_{0.3}O_3$ perovskite was coated with a mesoporous silica layer. Different $LaMn_{0.7}Fe_{0.3}O_{3.15}@mSiO_2$ carriers were prepared tuning the thickness of the mesoporous silica shell. These materials were then used in the fluidized-bed Chemical Reactor Engineering Centre (CREC) riser simulator and investigated as oxygen carriers for CLC application. Thus, this work addresses the following points: (1) $LaMn_{0.7}Fe_{0.3}O_{3.15}@mSiO_2$ nanoparticles are prepared with different shell thickness sizes. (2) $LaMn_{0.7}Fe_{0.3}O_3$ particles are stable in the silica shell at high temperatures under CLC conditions. (3) The solid-phase $LaMn_{0.7}Fe_{0.3}O_{3.15}$ within the $LaMn_{0.7}Fe_{0.3}O_{3.15}@mSiO_2$ structure is able to be reduced, providing an oxygen source under a nitrogen-free environment for methane combustion in CLC application. (4) The mesoporous silica shell provides stability with respect to sintering of $LaMn_{0.7}Fe_{0.3}O_{3.15}$ particles at high temperatures.

2. EXPERIMENTAL SECTION

2.1. Preparation of $LaMn_{0.7}Fe_{0.3}O_{3.15}$. The $LaMn_xFe_{1-x}O_3$ perovskite was prepared by the reactive grinding method using the single oxides (La_2O_3 and Mn_2O_3) as reactants.[36,37] The synthesis was performed in two steps. The oxide precursors were first calcined at 600 °C for 24 h and then introduced in a vial having 5 mm thick walls with three balls. The vial and balls are made of tempered steel. The vial was inserted in a SPEX laboratory grinder (rotation speed = 1040 rpm). At the end of this step, the single oxide conversion into perovskite was complete. The second step of grinding proceeded by adding an additive (ZnO) to increase the specific surface area of the perovskites. After milling, the ZnO was removed by leaching in 2 M NH_4Cl solution. Two additional washing operations were performed using distilled water to eliminate all of the NH_4Cl traces from the powder. Finally, the perovskite was calcined at 550 °C for 6 h. It should be noted that the presence of 30% Fe (as determined by atomic absorption) in the structure of perovskite was introduced through ball milling of reactant powders in tempered steel vials.[37]

2.2. Preparation of $LaMn_{0.7}Fe_{0.3}O_{3.15}@mSiO_2$. The $LaMn_{0.7}Fe_{0.3}O_{3.15}@mSiO_2$ composite was prepared according to the method reported in refs 38 and 39. A required amount of $LaMn_{0.7}Fe_{0.3}O_{3.15}$ perovskite was dispersed in a mixed solution containing cetyltrimethylammonium bromide (CTAB) (0.15 g), ammonia solution (0.25 mL, 28 wt %), ethanol (60 mL), and water (80 mL). The mixed suspension was homogenized for 0.5 h by ultrasonication. The ammonia solution was added as a catalyst for the synthesis because the rate of tetraethyl orthosilicate (TEOS) hydrolysis was not very high. In a typical synthesis, 0.05 mL of TEOS was added dropwise to the dispersion with continuous stirring. After reaction for at least 8 h, the product was collected by centrifugation at 5000 rpm for 15 min and then washed 4 times with water and ethanol. The product was dried at ambient temperature

for 12 h and then at 40 °C for another 12 h. Then, the powder was calcined at 550 °C for 6 h to remove the CTAB template. The synthesis procedure is shown in Figure 2.

2.3. Characterization of Oxygen Carriers. Phase identification of the prepared carriers was carried out by X-ray diffraction (XRD) using a Siemens D5000 with Cu Kα radiation (λ = 1.5406 Å). X-ray diffractograms were recorded with a step scan of 0.05° for 2θ between 15° and 75°. Phase recognition was obtained by comparison to Joint Committee on Powder Diffraction Standards (JCPDS) files. Particle sizes (D_1) were evaluated by means of the Scherrer equation after Warren's correction for instrumental broadening. Specific surface areas were calculated by the Brunauer−Emmett−Teller (BET) method from N_2 sorption isotherms, recorded at −196 °C using a Quantrachrome instrument. Before adsorption, samples were evacuated at 200 °C for 6 h to remove physisorbed water. Sample compositions were established by inductively coupled plasma (ICP) using a P40 instrument from Perkin-Elmer after dissolution of the catalyst in diluted HCl at 60 °C. Scanning electron microscopy (SEM) micrographs were obtained on a JEOL JSM-840 with an acceleration voltage of 15 kV. The samples were first dispersed on an aluminum stub and coated with an Au/Pd film. Transmission electron microscopy (TEM) images were recorded using a JEOL-2011 microscope operated at 200 kV.

A RXM-100 multicatalyst testing and characterization system (Advanced Scientific Design, Inc.) was used to perform temperature-programmed desorption of oxygen (TPD-O_2) and hydrogen temperature-programmed reduction (H_2-TPR) tests. For H_2-TPR experiments, 30 mg of solid sample was placed in a quartz reactor, pretreated under a flow of 20 mL min^{-1} (20% O_2 in He) at 550 °C for 2 h, and cooled to room temperature under a flow of He. The TPR was carried out under a 10 mL min^{-1} flow rate of 5% H_2 in Ar. The temperature was increased from 25 to 900 °C with a ramp of 5 °C min^{-1}. The consumption of hydrogen was monitored and quantified. For TPD-O_2, the same pretreatment was performed as for the TPR experiments. The solid (100 mg) was treated under the following conditions: 10 mL min^{-1} He and temperature from 25 to 900 °C with a ramp of 5 °C min^{-1}. To obtain a complete desorption, the solid was maintained at 900 °C for 10 min. A TCD was used for the quantification of oxygen. The amount of oxygen liberated was determined by deconvolution and integration of the desorption profile.

2.4. Reactivity and Stability Tests of Oxygen Carriers in the CREC Riser Simulator. The CREC riser simulator is a bench-scale (volume of ∼50 cm^3) mini-fluidized-bed reactor, developed at CREC, University of Western Ontario (UWO), London, Ontario, Canada.[40] A schematic diagram of the CREC riser simulator along with the gas injector is illustrated in Figure S1 of the Supporting Information.

For each reaction experiment in the CREC riser simulator, the required amount (maximum of 1 g) of solid oxygen carrier was first loaded into the reactor basket and the reactor was then closed. The desired temperature for the combustion reaction was set (limited to 700 °C in the riser simulator), and the system was heated under flowing argon to ensure that the reactor system was free from oxygen (air). Once the reactor reached the desired preset temperature, the argon flow was stopped and the pressure in the vacuum box was brought down to 17.2 kPa (2.5 psi) using a vacuum pump. The impeller was then turned on, and the feed (CH_4) was injected into the reactor using a preloaded syringe. At the end of the pre-specified reaction time, a valve isolating the reactor and the vacuum bottle was opened and the contents of the reactor were transferred to the vacuum

bottle. This caused an abrupt decrease of the reactor pressure, confirming that most of the reactant/product species were removed from the reactor almost instantaneously and that no further reaction took place. Finally, the product species were analyzed using a gas chromatograph (GC). Before the next cycle, the oxygen carrier was regenerated by flowing air at a specified temperature and during a preset reaction time.[41] This reduction−oxidation cycle was repeated 10 times to check the stability of the solid oxygen carriers under CLC conditions. The choice of this number of experimental cycles is a delicate issue because very large cycle numbers (say over 1000) would require very long experimentation, which most laboratories cannot afford.[12,24,41−44]

3. RESULTS AND DISCUSSION

3.1. Physical Properties. $LaMn_{0.7}Fe_{0.3}O_{3.15}@mSiO_2$ core−shell nanomaterials with different thicknesses of mesoporous silica shell were obtained by tuning the amount of TEOS in the silica deposition solution. The XRD patterns of all silica-coated perovskites exhibited similar diffraction peaks to that of $LaMnO_{3.15}$, confirming that the perovskite structure is retained (Figure 3). It was found that the diffraction peaks of two coated
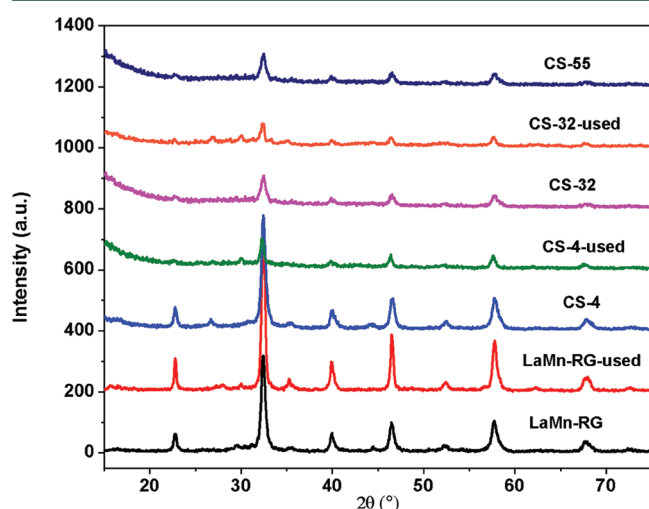

Figure 3. XRD patterns of $LaMn_{0.7}Fe_{0.3}O_3$ (LaMn-RG) perovskite and different $LaMn_{0.7}Fe_{0.3}O_{3.15}@mSiO_2$ core@shell (fresh and used after 10 reduction−oxidation cycles at 650 °C) nanoparticles.

perovskites (CS-32 and CS-55) had relatively low intensity compared to CS-4 and LaMn-RG because of the shielding effect of the silica shell to the X-rays. This effect is not perceptible for the CS-4 sample because it has a low thickness of silica of about 4 nm surrounding the perovskite agglomerates. The crystal domain size (Table 1) of all samples calculated by the Scherrer equation is about 24 nm.

The nitrogen adsorption−desorption isotherms of all oxygen carriers (Figure 4) show that the hysteresis disappears upon increasing the shell thickness and is completely vanished for sample CS-55. This means that mesoporous interparticular voids of the $LaMn_{0.7}Fe_{0.3}O_{3.15}$ perovskite disappear upon silica coating. This point will be further discussed below when reporting particle size changes. The BET specific surface areas of the samples (S_{BET}) were calculated from the isotherm analysis in the relative pressure range from 0.05 to 0.2, and the total pore volumes were calculated at $P/P_0 = 0.945$. The pore diameter of the samples was also determined using non-local density functional theory (NLDFT) calculations taking into account the adsorption branch (Figure 5). These values are

Table 1. Physical Properties of Prepared Oxygen Carriers

sample	shell thickness (nm)	crystal size (nm)	S_{BET} (m²/g)[a]	pore volume (cm³/g)[b]	pore diameter (nm)[c]
$LaMn_{0.7}Fe_{0.3}O_{3.15}$ (LaMn-RG)		24.2	37	0.111	11.6
CS-4	4 ± 1	25.2	73	0.104	4.4
CS-32	32 ± 3	24.1	96	0.078	3.8
CS-55	55 ± 5	24.0	102	0.065	2.5

[a]After calcination at 550 °C. [b]Volume of nitrogen adsorbed at $P/P_0 = 0.95$. [c]Determined by NLDFT calculations taking into account the adsorption branch.
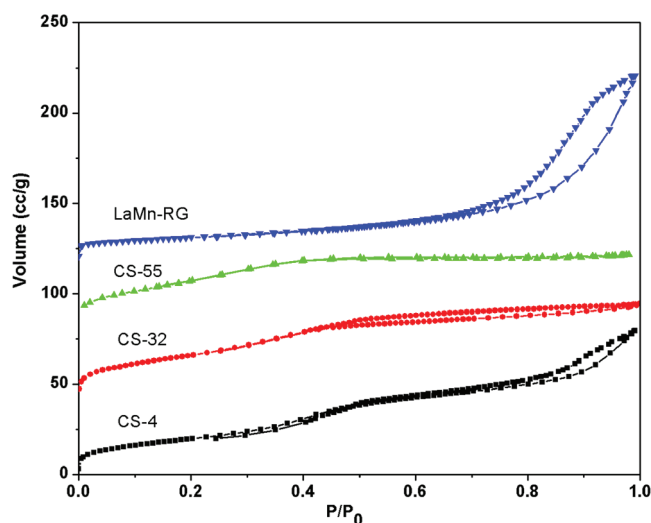

Figure 4. Nitrogen adsorption−desorption isotherms of the $LaMn_{0.7}Fe_{0.3}O_{3.15}$ and core@shell oxygen carriers measured at −196 °C.
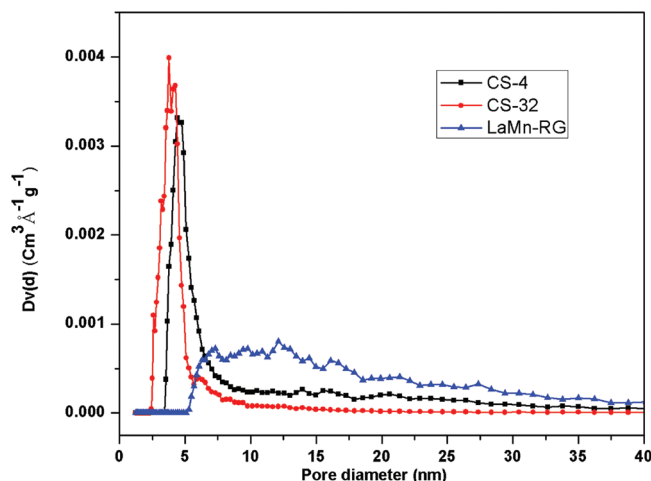

Figure 5. Pore size distribution of the prepared oxygen carriers.

reported in Table 1. The S_{BET} was increased from 73 to 102 m²/g as the mesoporous silica shell thickness of $LaMn_{0.7}Fe_{0.3}O_{3.15}@mSiO_2$ samples increased from 4 to 55 nm (see Figure S2 of the Supporting Information). Meng et al.[45] also observed an increase in S_{BET} by tuning mesoporous silica shell thickness in the preparation of mesoporous $Co_3O_4@mSiO_2$ core−shell material. On the contrary, the total pore volume and pore size of the $LaMn_{0.7}Fe_{0.3}O_{3.15}@mSiO_2$ materials were decreased, as compared to the parent

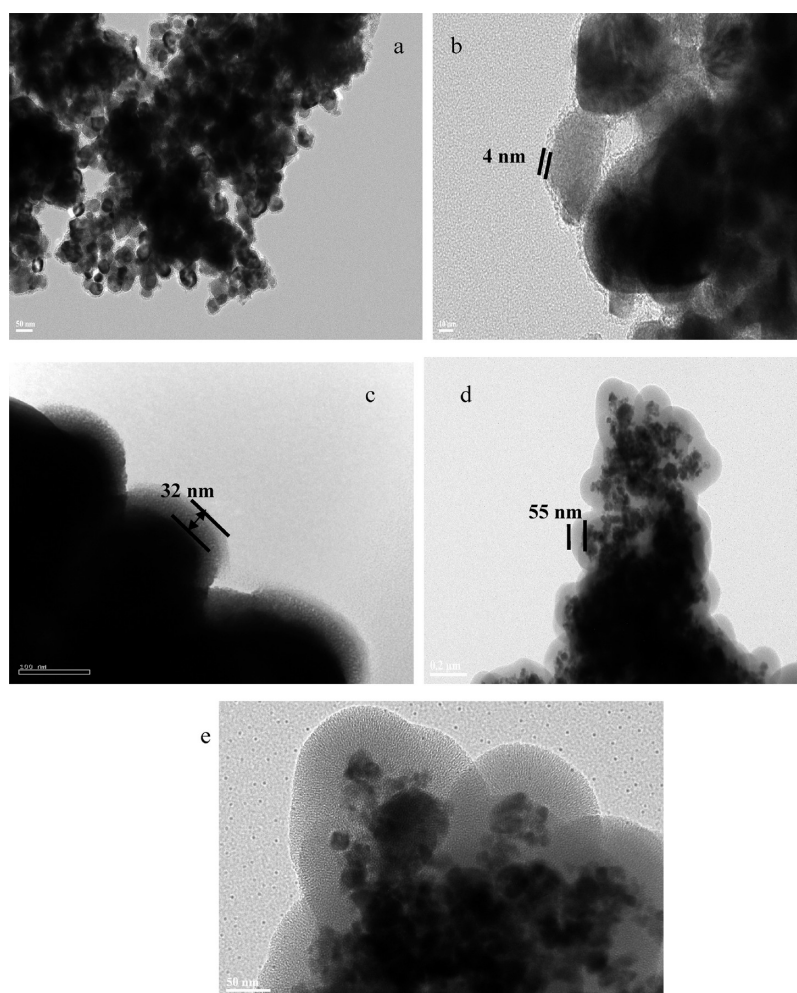**Figure 6.** TEM images of the (a) $LaMn_{0.7}Fe_{0.3}O_{3.15}$@mSiO$_2$ core@shell structure, (b) CS-4, (c) CS-32 (the scale bar is 0.2 μm), and (d and e) CS-55.

$LaMn_{0.7}Fe_{0.3}O_{3.15}$, and this reduction increases at thickening mesoporous silica shells (Table 1).

TEM images of the core−shell materials (Figure 6) show a typical core−shell structure with agglomerated $LaMn_{0.7}Fe_{0.3}O_{3.15}$ as a core and a distinct layer of mesoporous silica as a shell. The thickness of the mesoporous silica layers is uniform, containing an ordered silica mesostructure with cylindrical channels, which can be clearly observed in high-resolution transmission electron microscopy (HRTEM) (Figure 6e). The mesoporous SiO$_2$ shell on the $LaMn_{0.7}Fe_{0.3}O_{3.15}$ particles was formed by the surfactant templating process in a mixture of ethanol−water−ammonia. The cationic surfactant CTAB in solution, which can bind to the negatively charged particles of perovskite, interacts with the silicate oligomers produced from the hydrolysis and condensation of TEOS and assembles the ordered mesostructure (Figure 2).

3.2. H$_2$-TPR. The H$_2$-TPR profiles of $LaMn_{0.7}Fe_{0.3}O_{3.15}$ and $LaMn_{0.7}Fe_{0.3}O_{3.15}$@mSiO$_2$ are shown in Figure 7. It was mentioned in our previous studies that Mn-based perovskites present two main reduction steps.[22,46,47] The low-temperature step is attributed to the reduction of Mn^{3+} from the surface into Mn^{2+}, whereas the conversion of Mn^{3+} from the bulk into Mn^{2+} occurs during the second step. For Mn-based perovskite used in this study, as reported in ref 22, the first and second steps of

reduction are observed around 350 and 545 °C, respectively, while a small shoulder on the low-temperature side of the first peak corresponds to the reduction of some Mn^{4+} species. The presence of Mn^{4+} in LaMn-RG was also reported by Royer et al.[48] This small shoulder is observed for all perovskites prepared
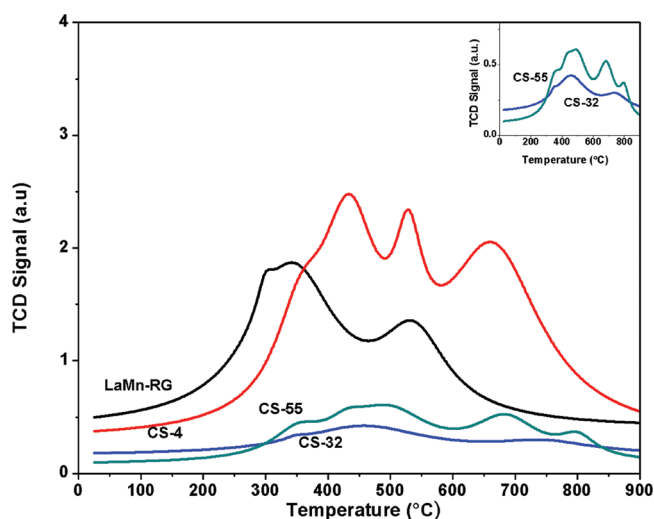

Figure 7. H$_2$-TPR profiles of the prepared oxygen carriers.

in this work (Figure 7). At this step, the reduction of Mn^{4+} to Mn^{3+} is started. The low-temperature peak of reduction is detected at 350 °C for $LaMn_{0.7}Fe_{0.3}O_{3.15}$, while it shifted to higher temperatures in the core−shell samples (430−460 °C). This peak is ascribed to the reduction of all Mn^{4+} to Mn^{3+}, while at the same time, reduction of Mn^{3+} into Mn^{2+} from the perovskite surface is started. The reaction corresponding to this step of reduction is

$$LaMn_{surf}{}^{3+}O_3 + \frac{1}{2}H_2 \rightarrow LaMn_{surf}{}^{2+}O_{2.5} + \frac{1}{2}H_2O \quad (3)$$

According to reaction 3, for complete reduction of Mn^{3+} to Mn^{2+}, 0.5 mol of H_2 is consumed during the first step of reduction; however, by integration of the TPR profiles, the amount of hydrogen consumption was 0.503, 0.538, 0.329, and 0.175 for LaMn-RG, CS-4, CS-55, and CS-32, respectively. In the case of LaMn-RG, the stoichiometric value is obtained within experimental error. The value of 0.538 in CS-4 is slightly above experimental error possibly because of the presence of some Mn^{4+} species in this sample. The effect of silica coating and some phase separation of silica in the core−shell-structured samples particularly for CS-32 led to a decreased reduction by hydrogen. The reduction seems to be more complicated in that case (Figure 7) because additional peaks are appearing in the core−shell sample profiles. Both low- and high-temperature signals of reduction were shifted to higher temperatures (400−600 °C for the first step of reduction and 600−800 °C for the second step of reduction) compared to the parent $LaMn_{0.7}Fe_{0.3}O_3$. The inset in Figure 7 clearly shows the reduction peaks of CS-32 and CS-55. The high-temperature peaks are ascribed to the reduction of Mn^{3+} into Mn^{2+} originating from the bulk of $LaMn_{0.7}Fe_{0.3}O_{3.15}$. Royer et al.[48] have performed some oxygen storage capacity measurements by alternative pulses of CO and O_2 under isothermal conditions up to 480 °C for $LaCoO_3$ and $LaMnO_{3.15}$, and they have evaluated the amount of oxygen immediately available by reduction of a perovskite. They found that, for $LaMnO_{3.15}$, it is possible to consume 0.15 (corresponding to the reduction of Mn^{4+}) and also 0.5 atoms of oxygen (corresponding to the reduction of all Mn^{3+} into Mn^{2+}). They have also shown that, upon reduction of all Mn^{3+} into Mn^{2+} (after the high-temperature reduction step), which leads to the formation of La_2O_3 and MnO, the reduction is reversible and the initial oxygen content of $LaMnO_{3.15}$ can be recovered easily by reoxidation of the reduced structure. The presence of 30% Fe in the structure of $LaMn_{0.7}Fe_{0.3}O_{3.15}$ has influenced reduction behavior of the samples. Because Fe^{3+} can be reduced even to the metallic state (Fe^0) at high temperatures, it could provide an additional source of oxygen available in this perovskite type.

3.3. TPD-O_2. The TPD-O_2 profiles of $LaMn_{0.7}Fe_{0.3}O_{3.15}$ and one of the core−shell oxygen carriers, CS-4, are shown in Figure 8. In agreement with some previous results,[22,46,47,49] these samples display two prominent characteristic peaks. The first peak, often referred to as α-oxygen, is ascribed to oxygen species adsorbed on the perovskite surface. The higher temperature desorption peak (above 700 °C; β-oxygen), is associated with the release of oxygen from the bulk of the perovskite. The latter desorbed amount is often considered as an indicator of the mobility of oxygen in the structure.[37,47] The amounts of α-O_2 and β-O_2 desorbed were calculated from the peak area by deconvolution of the O_2 desorption curves using Lorentzian peak shapes in a computer peak-fitting routine. Assuming that one monolayer of oxygen amounts to 4 μmol/
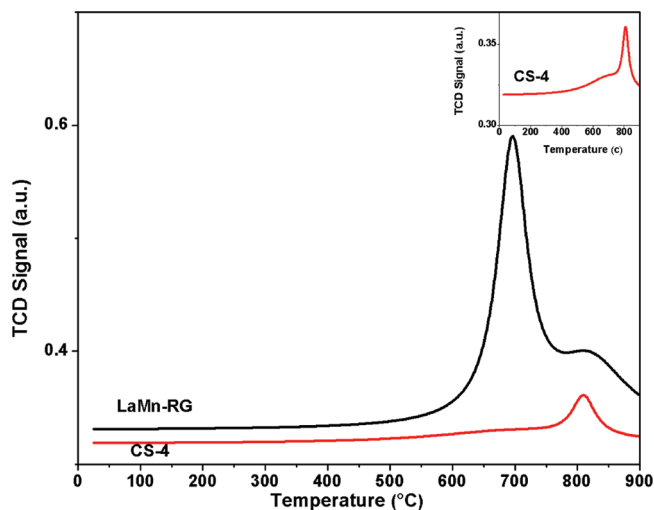
Figure 8. TPD-O_2 profiles of LaMn-RG and CS-4.

m^2, the number of moles of α-O_2 desorbed is also reported in terms of the desorbed monolayer (Table 2). It can be observed

Table 2. Amounts of Oxygen Desorbed during the TPD-O_2 Experiments

oxygen carrier	amount of oxygen desorbed (μmol/g)[a]		number of monolayers desorbed[b]	
	α-O_2	β-O_2	α-O_2	β-O_2
LaMn-RG	347	198	2.17	1.24
CS-4	121	55	0.76	0.34

[a]Calculated by deconvolution, with Lorentzian fitting, of the O_2 desorption curves. [b]Calculated by assuming 4 μmol/m^2 for one monolayer.

that perovskite-based oxygen carriers provide a high amount of α-oxygen, which is an essential parameter for initiation of the oxidation reaction. In the case of $LaMn_{0.7}Fe_{0.3}O_{3.15}$, the number of monolayers desorbed is about 2, which could originate from a high contribution of mobile oxygen from grain boundaries. The amount of oxygen desorbed from the CS-4 sample is lower compared to LaMn-RG (see Table 2), which should be due to the silica layer surrounding perovskite agglomerates changing the surface interaction of these particles with oxygen.

3.4. Reactivity and Stability Tests in the CREC Riser Simulator. The reactivity and stability of the prepared oxygen carrier particles under repeated reduction−oxidation were established in the CREC fluidized-bed riser simulator using CH_4 and air for the combustion and regeneration cycles, respectively. The combustion and regeneration processes were carried out at 550−650 °C and under atmospheric pressure. The contact time between fuel and oxygen carriers was varied between 10 and 50 s. The exit gas stream from the CREC riser simulator was analyzed using a MicroGC. It was mentioned in our previous work[22] that complete combustion of CH_4 into CO_2 and H_2O without formation of CO as a side product depends upon contact time between CH_4 and the oxygen carrier as well as the partial pressure of methane. This assertion will be further confirmed below. Therefore, the two parameters, total methane conversion and partial methane conversion to CO_2, are calculated from eqs 4 and 5

$$\gamma_{CH_4} = \frac{C_{CO_2} + C_{CO}}{C_{CH_4} + C_{CO_2} + C_{CO}} \times 100\% \tag{4}$$

$$\gamma_{CO_2} = \frac{C_{CO_2}}{C_{CH_4} + C_{CO_2} + C_{CO}} \times 100\% \tag{5}$$

where γ_{CH_4} and γ_{CO_2} are defined as the total conversion of CH_4 and partial methane conversion to CO_2, respectively, and C_i is the measured molar concentration of component i in the products.

The reactivity and stability tests of CS-4 and CS-32 core–shell-structured oxygen carriers demonstrated that the mesoporous silica shell did not limit the diffusion of the methane molecules to the active core and these materials were reactive enough compared to the core material (LaMn$_{0.7}$Fe$_{0.3}$O$_{3.15}$). It is clearly seen that total conversion of methane (solid lines in Figure 9) for all types of oxygen carriers studied in this work is
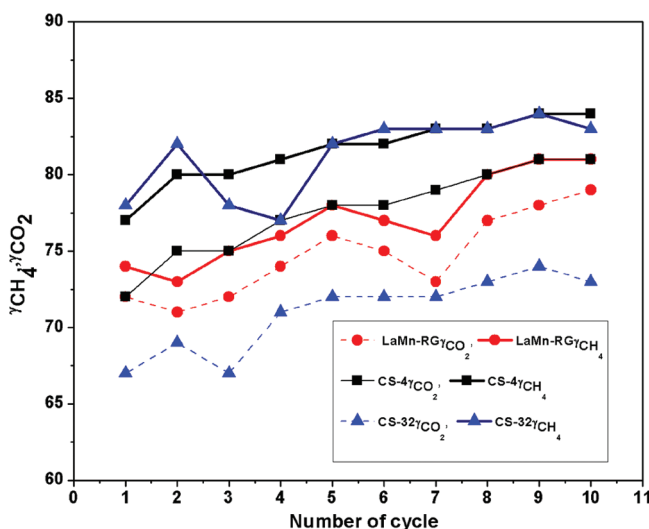

Figure 9. Total and partial conversions of methane over LaMn$_{0.7}$Fe$_{0.3}$O$_{3.15}$ and LaMn$_{0.7}$Fe$_{0.3}$O$_{3.15}$@mSiO$_2$ oxygen carriers in multiple CLC cycles in the CREC fluidized-bed riser simulator (T, 650 °C; P, 1 atm; $W_{carrier}$, 0.3 g; $V_{CH_4,inj}$, 10 mL; and t, 50 s).

higher compared to partial methane conversion (dotted line in Figure 9). The difference between total and partial methane conversions is due to the formation of CO during combustion. The lower this difference, the higher the conversion to the complete combustion product (CO$_2$). Both partial and total conversions of methane over the CS-4 carrier are relatively higher compared to the parent LaMn$_{0.7}$Fe$_{0.3}$O$_{3.15}$ carrier. Furthermore, it seems that LaMn$_{0.7}$Fe$_{0.3}$O$_3$@mSiO$_2$ oxygen carriers, particularly CS-4, display a higher stability in methane conversion under CLC conditions during 10 reduction–oxidation cycles than the LaMn$_{0.7}$Fe$_{0.3}$O$_{3.15}$ carrier. Indeed, the higher reactivity and stability of the core–shell oxygen carriers may be a result of the partial core–shell structure of these materials, in which the LaMn$_{0.7}$Fe$_{0.3}$O$_{3.15}$ core is surrounded by a mesoporous silica shell.

Figure 10 shows the selectivity of CO and CO$_2$ for the combustion of methane under CLC conditions in the riser simulator as a function of redox cycle number for LaMn-RG, CS-4, and CS-32 carriers. The formation of CO is due to the reforming reaction of methane with CO$_2$ and/or H$_2$O. The CO
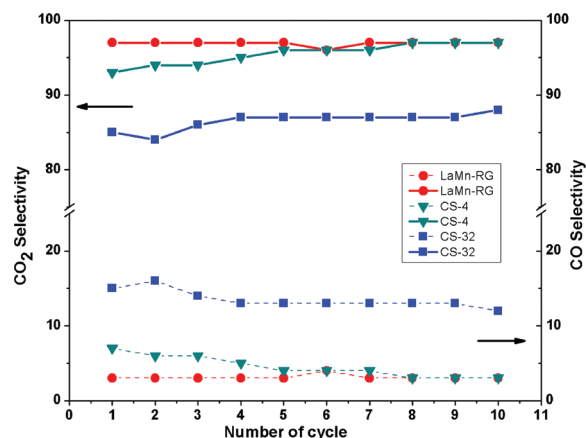

Figure 10. Selectivity of CO$_2$ and CO for combustion of methane over LaMn$_{0.7}$Fe$_{0.3}$O$_{3.15}$ and LaMn$_{0.7}$Fe$_{0.3}$O$_{3.15}$@mSiO$_2$ oxygen carriers in multiple CLC cycles in the CREC fluidized-bed riser simulator (T, 650 °C; P, 1 atm; $W_{carrier}$, 0.3 g; $V_{CH_4,inj}$, 10 mL; and t, 50 s).

and CO$_2$ selectivity terms were calculated, according to eqs 6 and 7.

$$\text{selectivity of CO} = \frac{C_{CO}}{C_{CO_2} + C_{CO}} \times 100\% \tag{6}$$

$$\text{selectivity of CO}_2 = \frac{C_{CO_2}}{C_{CO_2} + C_{CO}} \times 100\% \tag{7}$$

Figure 10 demonstrates that the amount of CO formed is small when using the LaMn$_{0.7}$Fe$_{0.3}$O$_3$@mSiO$_2$ oxygen carrier. The selectivity toward CO is much lower when using LaMn-RG as a carrier than core–shell structures. Increasing the silica shell thickness in LaMn$_{0.7}$Fe$_{0.3}$O$_{3.15}$@mSiO$_2$ carriers leads to higher selectivity of methane combustion toward CO. In the case of LaMn-RG, average CO selectivity (ACS) is 3%, which is comparable to CS-4 with ACS of 5%. CS-32 with ACS of 13% showed a higher tendency toward CO formation during repeated cycles in the riser simulator. As discussed in our previous work, the formation of CO in CLC conditions using the perovskite oxygen carriers is strongly dependent upon the experimental process conditions, such as the partial pressure of methane in feed and the contact time between the oxygen carrier and gas reactant, which affect the degree of reduction of the oxygen carrier.[22] The effects of these two factors are discussed in more detail in the following sections for CH$_4$ conversion and CO formation under CLC conditions in the riser simulator.

3.4.1. Oxygen Balance. The results of oxygen balance for each carrier at each reduction–reoxidation cycle are reported in Table 3. The total oxygen content of each perovskite is obtained considering the reduction of all Mn^{4+} and Mn^{3+} to Mn^{2+} from the surface and bulk of perovskite as well as the reduction of Fe^{3+} to Fe^0 (see the H2-TPR section). In addition, a contribution of α-oxygen calculated from TPD-O$_2$ data is added to the total available oxygen in solid, which is also an effective factor for the oxidation reaction. The oxygen consumed at each redox cycle is calculated using the total and partial CH$_4$ conversion for the production of CO$_2$ and CO at each cycle. The results in Table 3 illustrate the fact that the amount of oxygen consumed at each cycle is satisfactorily stable, which is an additional indication for high stability of these perovskite-based oxygen carriers. Although the sample

Table 3. Comparison of the Oxygen Balance in LaMn-RG, CS-4, and CS-32[a]

carrier	total oxygen content in the carrier ($\times 10^5$, mol of O_2)	oxygen consumed at each cycle ($\times 10^5$, mol of O_2)									
		1	2	3	4	5	6	7	8	9	10
LaMn-RG	114	29.8	29.4	30.0	30.6	31.4	31.0	30.4	32.1	32.5	32.7
CS-4	107	30.4	31.7	31.7	32.3	32.7	32.7	33.1	33.3	33.7	33.7
CS-32	105	29.6	30.8	29.6	30.2	31.4	31.7	31.7	31.9	32.3	32.1

[a]Mass of perovskite = 0.3 g.

CS-4 has slightly lower available oxygen content compared to LaMn-RG (11.4 wt % compared to 12.2 wt %), its oxygen consumed at each cycle is higher than that of LaMn-RG. This could suggest that some interaction of the mesoporous silica shell with the perovskite core results in a slight improvement in the overall amount and/or rate of oxygen available for methane combustion.

The three experiments reported in Table 3 all show about a 10% increase in oxygen extracted from the perovskite core as a function of the number of reduction−oxidation cycles. This may be associated with some minor enhancement of oxygen mobility in perovskite grain boundaries with no major change in perovskite particle morphology.

3.4.2. Effect of the Contact Time between the Feed (CH_4) and Oxygen Carrier. The behavior of the CS-4 oxygen carrier for combustion of 10 mL of CH_4 at 650 °C was investigated by varying the contact time between methane and the oxygen carrier. Figure 11 shows that increasing the contact time
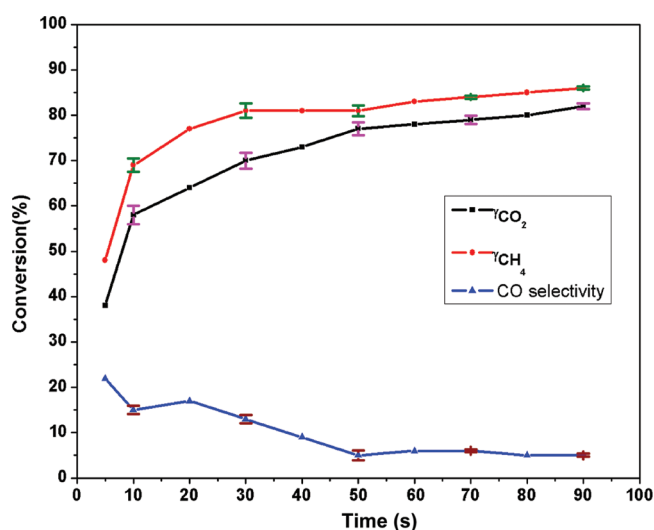

Figure 11. Total and partial conversions of methane and CO selectivity variations versus contact time over the CS-4 oxygen carrier in the CREC riser simulator (*T*, 650 °C; *P*, 1 atm; $W_{carrier}$, 0.3 g; and $V_{CH_4,inj}$, 10 mL).

between the reactant (CH_4) and carrier material results as expected in augmentation of both total and partial CH_4 conversions. The rate of this increase in both conversions was noticeably significant between 10 and 30 s, but at higher contact time, the conversions increased very slowly. CO_2 is likely produced by the reaction between methane and oxygen species mainly located at surface anionic vacancies after the reaction of lattice oxygen from the surface. When the oxygen species on the surface of perovskite are consumed, higher concentrations of surface oxygen vacancies are produced, and

this provides pathways for oxygen transport through the adjacent layers in the lattice and enhances the diffusivity of oxygen.[50] The amount of oxygen migrating from the bulk to the surface increases with the rising contact time, and more CO_2 could be formed by selective oxidation of CH_4. Therefore, the partial conversion of methane to CO_2 increases to reach 82% at *t* of 90 s. The total conversion of methane also increased with a rising contact time and reached 86% at *t* of 90 s. The role of oxygen migration from the bulk to the surface for producing CO_2 should be more pronounced at long contact time. The nonzero increase in CH_4 conversion at high contact time therefore suggests that diffusion of oxygen from the bulk is still occurring in these experimental conditions.

An unexpected trend is observed for CO selectivity because a higher CO formation rate was expected with a rising contact time because CO production should be associated with the oxygen-depleted carrier with a high degree of reduction. One possible reason for the reduction of the CO concentration could be the occurrence of the water−gas shift reaction according to reaction 8.

$$CO + H_2O \Leftrightarrow CO_2 + H_2 \tag{8}$$

In fact, at long contact time as the reaction proceeds, the partially reduced oxygen carrier catalyzes the water−gas shift reaction, leading to the conversion of more CO to CO_2. The Fe species present in high concentration in the perovskite structure should be catalytically active in this reaction.[51] In addition the higher partial pressure of water will favor the water−gas shift reaction (eq 8). Song et al.[52] have also reported the generation of a small concentration of CO and H_2 for CH_4 combustion over $CaSO_4$ oxygen carriers under CLC conditions at a short reduction period.

3.4.3. Effect of the Partial Pressure of CH_4. Results of total and partial conversions of methane as well as CO selectivity at varying partial pressures of methane are shown in Figure 12. It can be observed that both conversions and CO selectivity increase by raising the volume of methane injected in the reactor, which results in increasing P_{CH_4}. The higher the P_{CH_4}, the more oxygen from the surface, grain boundaries, and lattice is released and reacted with methane, leading to increased CH_4 conversion, as a result of the increased oxidation rate.

3.4.4. Effect of the Reaction Temperature. Increasing the reactor temperature results in increasing both total and partial conversions of methane and declining CO selectivity (Figure 13). Thus, a high reaction temperature favors both oxidation and water−gas shift reaction rates. Indeed, the mobility of the lattice oxygen of the perovskite-based oxygen carriers plays an important role in the oxidation of methane under CLC conditions. This mobility as well as the migration rate of oxygen from the bulk to the surface during methane combustion over $LaMn_{0.7}Fe_{0.3}O_3$ is strongly affected by the temperature. In other words, the oxygen vacancies can be formed easily when
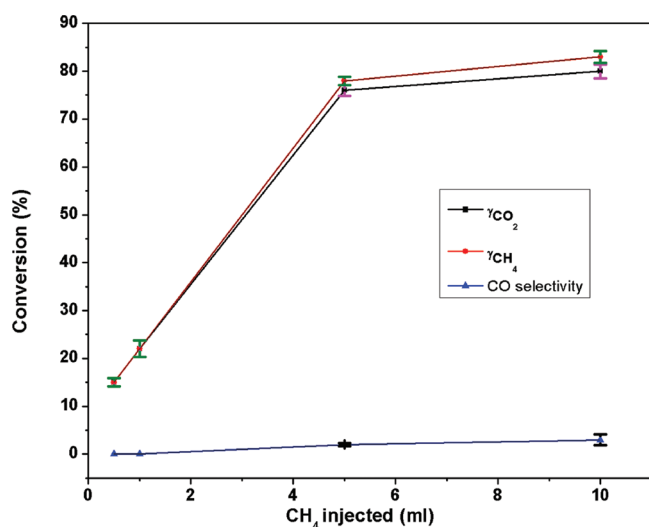
Figure 12. Total and partial conversions of methane and CO selectivity variations versus methane partial pressure over the CS-4 oxygen carrier in the CREC riser simulator (T, 650 °C; P, 1 atm; $W_{carrier}$, 0.3 g; $V_{CH_4,inj}$, 10 mL; and t, 50 s).
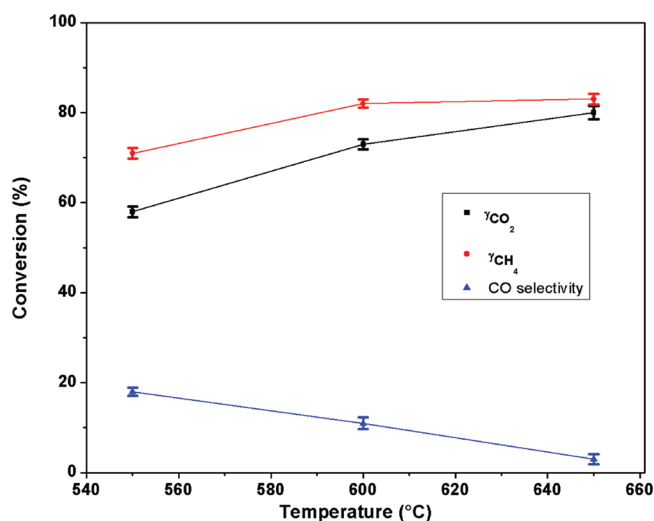

Figure 13. Total and partial conversions of methane and CO selectivity variations versus different reaction temperatures over the CS-4 oxygen carrier in the CREC riser simulator (T, 650 °C; P, 1 atm; $W_{carrier}$, 0.3 g; $V_{CH_4,inj}$, 10 mL; and t, 50 s).

perovskite is heated at a higher temperature, and consequently, more oxygen species will be available for the CH_4 reaction, owing to the increased oxygen diffusivity.

At higher temperatures, the water–gas shift reaction is faster, leading to a higher conversion of CO to CO_2. Therefore, operating the CLC process at a high temperature is beneficial, improving the rate of the reaction and reactivity of the carrier as well as minimizing the CO formation. Too high a temperature however results in agglomeration of pure perovskite particles, which causes some deactivation and defluidization of particles during CLC cycles.

3.5. Physical Properties of the Used Oxygen Carriers. The oxygen carriers after 10 repeated redox cycles in the CREC riser simulator were again characterized by different techniques, such as XRD, SEM, and TEM. The XRD patterns of oxygen carriers used in the CREC riser simulator after 10 cycles (Figure 3) show that the crystal structure of all perovskites

remained unchanged after 10 reduction–oxidation cycles. No peak corresponding to lanthanum or manganese silicates was observed on the XRD patterns. This indicates that there is no chemical interaction between the $LaMn_{0.7}Fe_{0.3}O_3$ core and the silica shell and consequently proves that the core–shell structure of $LaMn_{0.7}Fe_{0.3}O_3$@$mSiO_2$ oxygen carriers is maintained after 10 CLC redox cycles.

SEM images of fresh and used (after 10 redox cycles) oxygen carriers are presented in Figure 14. The images of fresh samples (left side images in Figure 14) show that core@shell materials are composed of elementary particles agglomerated to the size of 4–12 μm. The average particle size of the samples derived from the analysis of SEM images is reported in Table 4. The particle size of the $LaMn_{0.7}Fe_{0.3}O_{3.15}$@$mSiO_2$ oxygen carriers is smaller than that of the parent $LaMn_{0.7}Fe_{0.3}O_{3.15}$ (22 μm), which could be due to ultrasonication of the particles during the preparation of the core–shell material. Moreover, it was found that the average particle size of the core–shell significantly decreased with the increase of the shell thickness. Because the sonification conditions were identical for the three core–shell samples, it seems that some agglomerate dissociation is initiated during shell formation. It could also be observed that the morphology of the used oxygen carriers was not severely affected after 10 CLC cycles, in both cases of $LaMn_{0.7}Fe_{0.3}O_{3.15}$ and $LaMn_{0.7}Fe_{0.3}O_{3.15}$@$mSiO_2$ materials. Comparing the average particle size for fresh and used samples reveals that there is an increase in the particle size of all carriers, indicating that some agglomeration occurs during the 10 repeated cycles of CLC. This increase is significantly lower for the core–shell materials than for $LaMn_{0.7}Fe_{0.3}O_{3.15}$. This illustrates the protective role of the mesoporous silica shell around the $LaMn_{0.7}Fe_{0.3}O_{3.15}$ core, which noticeably decreases the sintering of oxygen carrier particles.

As mentioned in this work, $LaMn_xFe_{1-x}O_{3.15}$@$mSiO_2$ are beneficial as carriers for the CLC process working at temperatures below 700 °C.[5,22,35,41,42,53,54] The CLC process working at higher temperatures (>800 °C) yields higher turbine thermal efficiencies. CLC oxygen carriers working at such higher temperatures are therefore also of interest. The principle of protecting the carrier with a shell of mesostructured material, demonstrated here with a silica shell, is currently being explored in our laboratory, using more refractory oxide shells compared to silica. Silica shells are known however for some softening around 800 °C, leading to some sintering in the fluidized bed.

TEM images of used oxygen carriers (Figure 15) show that the mesoporous silica shell is indeed intact after 10 cycles of CLC, and no changes in the structure and thickness of the silica shell are observed.

4. CONCLUSION

Three $LaMn_{0.7}Fe_{0.3}O_{3.15}$@$mSiO_2$ samples with different thicknesses of silica shell were obtained by tuning the concentration of the TEOS silica precursor in the gel. When this parameter was increased, the thickness of the ordered mesoporous silica shell and BET surface area increased. TPD-O_2 and H_2-TPR results showed a lower amount of α- and β-oxygen and more complex reduction behavior for core–shell materials compared to the parent core ($LaMn_{0.7}Fe_{0.3}O_3$). They presented however a higher reactivity toward methane and better stability over 10 redox cycles (Figure 9). This is due to the protective role against sintering of the mesoporous silica shells surrounding the perovskite core particles. It was indeed confirmed by SEM images that agglomeration of the particles during repeated
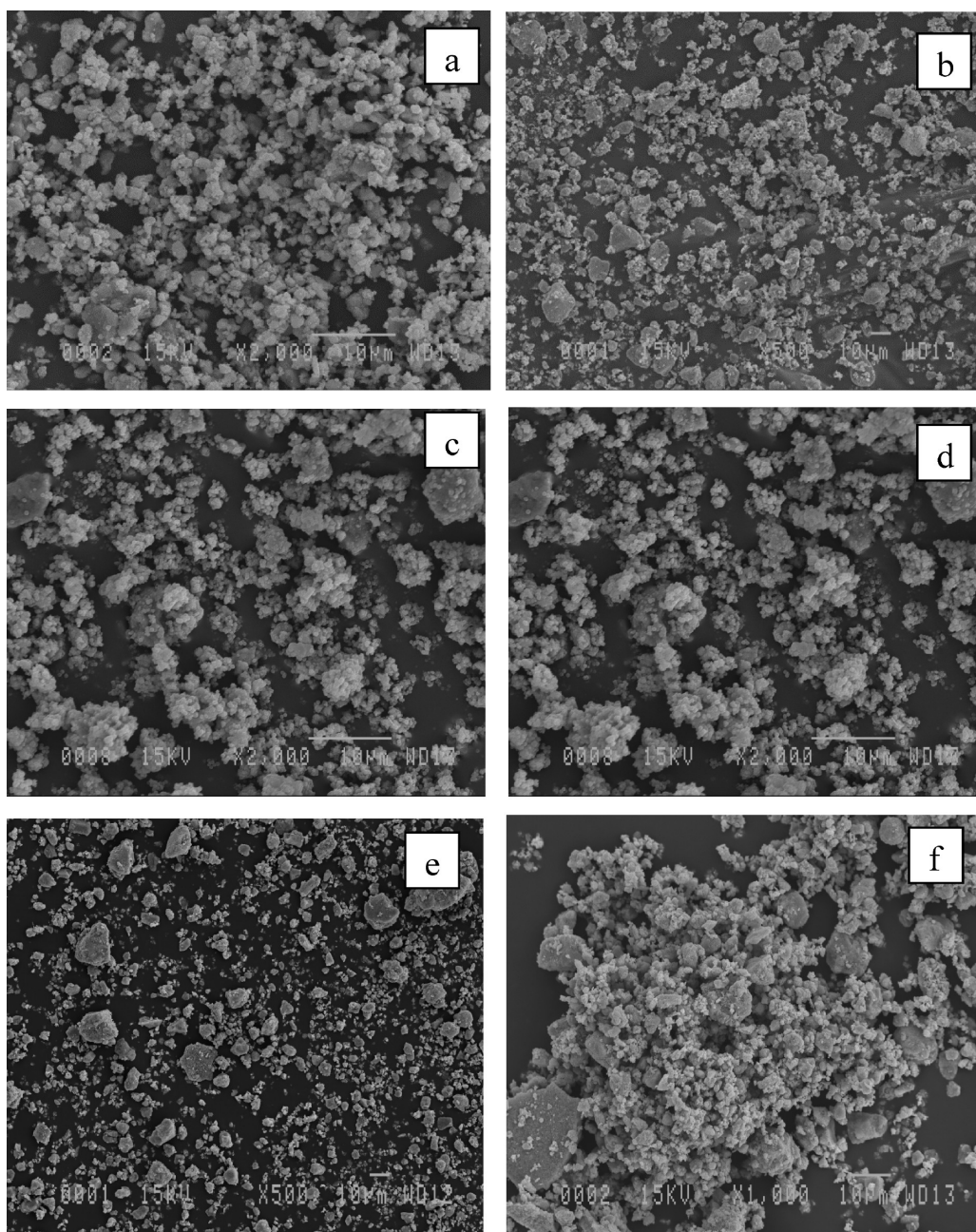
Figure 14. SEM images of (left side) fresh and (right side) used (a and b) CS-4, (c and d) CS-32, and (e and f) LaMn-RG.

Table 4. Particle Sizes of the Fresh and Used Oxygen Carriers Obtained from SEM Images

carrier	average particle size of fresh samples (μm)	average particle size of used samples (μm)
LaMn-RG	22	75
CS-4	12	17
CS-32	8	8
CS-55	4	

cycles was significantly better controlled using core−shell oxygen carriers. Interestingly, this increased resistance to agglomeration and reactivity was not obtained at the expense of CO_2 selectivity, especially at low shell thickness. In Figure 10, it is indeed found that the CO_2 and CO selectivities observed with sample CS-4 match the selectivity of sample

LaMn-RG after a few cycles. Both total methane conversion and partial conversion of CH_4 to CO_2 increased with a rising contact time because more surface α-oxygens as well as oxygen from grain boundaries and bulk of perovskites could participate in the combustion of a determined amount of methane. The selectivity of CO was however reduced, owing to the increased water−gas shift conversion. The same increasing trend was observed for both conversions by rising the partial pressure of methane and reaction temperature.

These combustion tests confirm the stability of perovskite morphology upon repeated reduction−oxidation cycles. This is associated with both the well-documented ability of perovskite oxides to afford large deviation to oxygen stoichiometry and the high mobility of oxygen species present in crystal domain boundaries.[38,44] The exchange of both types of oxygen does not affect crystal symmetry and particle morphology.
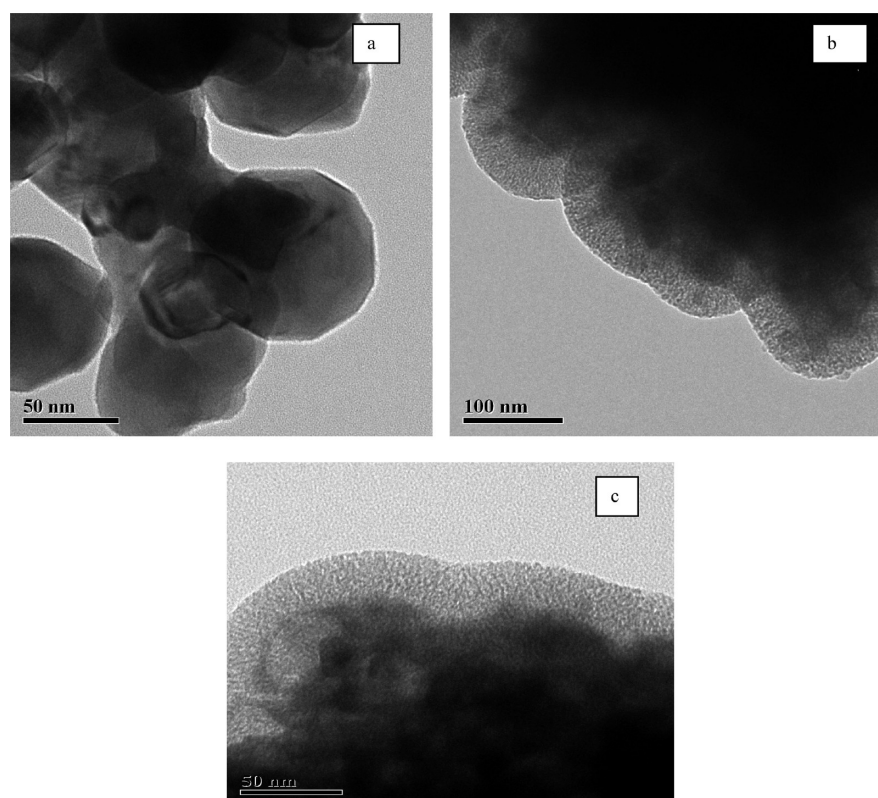
Figure 15. TEM images of (a) CS-4 and (b and c) CS-32 after 10 redox cycles (at 650 °C) in the CREC riser simulator.

The XRD results of core−shell carriers used during 10 repeated redox cycles confirmed that the crystalline structure of the perovskite remained unchanged. Furthermore, TEM images of the used carriers also demonstrated that there was no change in the mesostructure and thickness of the silica shell. Consequently, $LaMn_{0.7}Fe_{0.3}O_3@mSiO_2$ oxygen carriers are interesting solid carriers for CLC because of their high reactivity in methane combustion and high oxygen storage capacity and stability during repeated redox cycles.

ASSOCIATED CONTENT

ⓢ Supporting Information

The CREC riser simulator consists of two sections: the upper and lower shells. The lower shell includes both the injection port and catalyst basket. The catalyst basket is designed to fit inside the annular space of the bottom shell. Each of the shells has its own set of heaters. An impeller is located in the upper section, and upon rotation of the impeller at high speeds (up to 5000 rpm), the gas is forced both outward in the impeller section and downward in the outer reactor annulus, causing the solids catalyst to become fully fluidized. Schematic diagram of the CREC riser simulator experimental setup (Figure S1)[39] and dependence of S_{BET} on the mesoporous silica shell thickness in $LaMnO_{3.15}@mSiO_2$ oxygen carriers (Figure S2). This material is available free of charge via the Internet at http://pubs.acs.org.

AUTHOR INFORMATION

Corresponding Author
*E-mail: serge.kaliaguine@gch.ulaval.ca.

Notes
The authors declare no competing financial interest.

REFERENCES

(1) Mikkelsen, M.; Jørgensen, M.; Krebs, F. C. *Energy Environ. Sci.* **2009**, *3*, 43−81.

(2) Olajire, A. A. *Energy* **2010**, *35*, 2610−2628.

(3) Naqvi, R.; Bolland, O. *Int. J. Greenhouse Gas Control* **2007**, *1*, 19−30.

(4) Ritcher, H. J.; Knoche, K. F. Reversibility of combustion processes. In *Efficiency and Costing*; American Chemical Society (ACS): Washington, D.C., 1983; ACS Symposium Series, Vol. 235, Chapter 3, pp 71−85.

(5) Hossain, M. M.; de Lasa, H. I. *Chem. Eng. Sci.* **2008**, *63*, 4433−4451.

(6) Ishida, M.; Jin, H. *Ind. Eng. Chem. Res.* **1996**, *35*, 2469−2472.

(7) Abad, A.; Mattisson, T.; Lyngfelt, A.; Rydén, M. *Fuel* **2006**, *85*, 1174−1185.

(8) Håkonsen, S. F.; Blom, R. *Environ. Sci. Technol.* **2011**, *45*, 9619−9626.

(9) Lyngfelt, A.; Leckner, B.; Mattisson, T. *Chem. Eng. Sci.* **2001**, *56*, 3101−3113.

(10) Adánez, J.; de Diego, L. F.; García-Labiano, F.; Gayán, P.; Abad, A.; Palacios, J. M. *Energy Fuels* **2004**, *18*, 371−377.

(11) Mattisson, T.; Johansson, M.; Lyngfelt, A. *Energy Fuels* **2004**, *18*, 628−637.

(12) Villa, R.; Cristiani, C.; Groppi, G.; Lietti, L.; Forzatti, P.; Cornaro, U.; Rossini, S. *J. Mol. Catal. A: Chem.* **2003**, *204−205*, 637−646.

(13) Jerndal, E.; Mattisson, T.; Lyngfelt, A. *Energy Fuels* **2009**, *23*, 665−676.

(14) Dueso, C.; Abad, A.; García-Labiano, F.; de Diego, L. F.; Gayán, P.; Adánez, J.; Lyngfelt, A. *Fuel* **2010**, *89*, 3399−3409.

(15) Arjmand, M.; Azad, A.-M.; Leion, H.; Lyngfelt, A.; Mattisson, T. *Energy Fuels* **2011**, *25*, 5493−5502.

(16) de Diego, L. F.; García-Labiano, F.; Gayán, P.; Celaya, J.; Palacios, J. M.; Adánez, J. *Fuel* **2007**, *86*, 1036−1045.

(17) Gayán, P.; Forero, C. R.; Abad, A.; de Diego, L. F.; García-Labiano, F.; Adánez, J. *Energy Fuels* **2011**, *25*, 1316−1326.

(18) Gayán, P.; Forero, C. R.; de Diego, L. F.; Abad, A.; García-Labiano, F.; Adánez, J. *Int. J. Greenhouse Gas Control* **2010**, *4*, 13−22.

(19) Cuadrat, A.; Abad, A.; García-Labiano, F.; Gayán, P.; de Diego, L. F.; Adánez, J. *Int. J. Greenhouse Gas Control* **2011**, *5*, 1630−1642.

(20) Adánez, J.; Cuadrat, A.; Abad, A.; Gayán, P.; de Diego, L. F.; García-Labiano, F. *Energy Fuels* **2010**, *24*, 1402−1413.

(21) Zafar, Q.; Abad, A.; Mattisson, T.; Gevert, B.; Strand, M. *Chem. Eng. Sci.* **2007**, *62*, 6556−6567.

(22) Sarshar, Z.; Kleitz, F.; Kaliaguine, S. *Energy Environ. Sci.* **2011**, *4*, 4258−4269.

(23) Readman, J. E.; Olafsen, A.; Larring, Y.; Blom, R. *J. Mater. Chem.* **2005**, *15*, 1931−1937.

(24) Rydén, M.; Lyngfelt, A.; Mattisson, T.; Chen, D.; Holmen, A.; Bjørgum, E. *Int. J. Greenhouse Gas Control* **2008**, *2*, 21−36.

(25) Leion, H.; Larring, Y.; Bakken, E.; Bredesen, R.; Mattisson, T.; Lyngfelt, A. *Energy Fuels* **2009**, *23*, 5276−5283.

(26) Bakken, E.; Norby, T.; Stølen, S. *Solid State Ionics* **2005**, *176*, 217−223.

(27) Fossdal, A.; Bakken, E.; Øye, B. A.; Schøning, C.; Kaus, I.; Mokkelbost, T.; Larring, Y. *Int. J. Greenhouse Gas Control* **2011**, *5*, 483−488.

(28) Paulus, U. A.; Endruschat, U.; Feldmeyer, G. J.; Schmidt, T. J.; Bönnemann, H.; Behm, R. J. *J. Catal.* **2000**, *195*, 383−393.

(29) Zhong, C.-J.; Luo, J.; Njoki, P. N.; Mott, D.; Wanjala, B.; Loukrakpam, R.; Lim, S.; Wang, L.; Fang, B.; Xu, Z. *Energy Environ. Sci.* **2008**, *1*, 454−466.

(30) Zhong, C. J.; Maye, M. M. *Adv. Mater.* **2001**, *13*, 1507−1511.

(31) Park, J.; Forman, A. J.; Tang, W.; Cheng, J.; Hu, Y.; Lin, H.; McFarland, E. W. *Small* **2008**, *4*, 1694−1697.

(32) Park, J.-N.; McFarland, E. W. *J. Catal.* **2009**, *266*, 92−97.

(33) Joo, S. H.; Park, J. Y.; Tsung, C.-K.; Yamada, Y.; Yang, P.; Somorjai, G. A. *Nat. Mater.* **2009**, *8*, 126−131.

(34) Epherre, R.; Duguet, E.; Mornet, S.; Pollert, E.; Louguet, S.; Lecommandoux, S.; Schatz, C.; Goglio, G. *J. Mater. Chem.* **2011**, *21*, 4393−4401.

(35) Park, J.-N.; Zhang, P.; Hu, Y.-S.; McFarland, E. W. *Nanotechnology* **2010**, *21*, 225708.

(36) Kaliaguine, S.; Van Neste, A. Process for synthesizing perovskites using high energy milling. U.S. Patent 6,017,504, 2000.

(37) Kaliaguine, S.; Van Neste, A.; Szabo, V.; Gallot, J. E.; Bassir, M.; Muzychuk, R. *Appl. Catal., A* **2001**, *209*, 345−358.

(38) Deng, Y.; Qi, D.; Deng, C.; Zhang, X.; Zhao, D. *J. Am. Chem. Soc.* **2007**, *130*, 28−29.

(39) Guo, X.; Deng, Y.; Gu, D.; Che, R.; Zhao, D. *J. Mater. Chem.* **2009**, *19*, 6706−6712.

(40) De Lasa, H. I. Novel riser reactor simulator. U.S. Patent 5,102,628, 1992.

(41) Hossain, M. M.; de Lasa, H. I. *AIChE J.* **2007**, *53*, 1817−1829.

(42) Sedor, K. E.; Hossain, M. M.; de Lasa, H. I. *Chem. Eng. Sci.* **2008**, *63*, 2994−3007.

(43) Zafar, Q.; Mattisson, T.; Gevert, B. *Energy Fuels* **2005**, *20*, 34−44.

(44) Li, F.; Sun, Z.; Luo, S.; Fan, L.-S. *Energy Environ. Sci.* **2011**, *4*, 876−880.

(45) Meng, Y.; Chen, D.; Jiao, X. *J. Phys. Chem. B* **2006**, *110*, 15212−15217.

(46) Royer, S.; Bérubé, F.; Kaliaguine, S. *Appl. Catal., A* **2005**, *282*, 273−284.

(47) Royer, S.; Duprez, D.; Kaliaguine, S. *Catal. Today* **2006**, *112*, 99−102.

(48) Royer, S.; Alamdari, H.; Duprez, D.; Kaliaguine, S. *Appl. Catal., B* **2005**, *58*, 273−288.

(49) Levasseur, B.; Kaliaguine, S. *Appl. Catal., B* **2009**, *88*, 305−314.

(50) Dai, X. P.; Li, R. J.; Yu, C. C.; Hao, Z. P. *J. Phys. Chem. B* **2006**, *110*, 22525−22531.

(51) Watanabe, K.; Miyao, T.; Higashiyama, K.; Yamashita, H.; Watanabe, M. *Catal. Commun.* **2009**, *10*, 1952−1955.

(52) Song, Q.; Xiao, R.; Deng, Z.; Zhang, H.; Shen, L.; Xiao, J.; Zhang, M. *Energy Convers. Manage.* **2008**, *49*, 3178−3187.

(53) Hossain, M. M.; de Lasa, H. I. *Chem. Eng. Sci.* **2010**, *65*, 98−106.

(54) Sedor, K. E.; Hossain, M. M.; de Lasa, H. I. *Can. J. Chem. Eng.* **2008**, *86*, 323−334.